Dichroism in the Interaction between Vortex Electron Beams, Plasmons, and Molecules

A. Asenjo-Garcia[1] and F. J. García de Abajo[1,2,*]
[1]ICFO-Institut de Ciencies Fotoniques, Mediterranean Technology Park, 08860 Castelldefels (Barcelona), Spain
[2]ICREA-Institució Catalana de Recerca i Estudis Avançats, Passeig Lluís Companys 23, 08010 Barcelona, Spain
(Received 12 December 2013; revised manuscript received 8 March 2014; published 6 August 2014)

We study the transfer of orbital angular momentum between vortex electron beams and chiral samples, such as staircase plasmonic nanostructures and biomolecules. Inelastic electron scattering from these samples produces large dichroism in the momentum-resolved electron energy-loss spectra. We illustrate this phenomenon with calculations for chiral and nonchiral clusters of silver spheres using both focused and extended electron beams, which exhibit ~10% difference between channels of opposite angular momentum. In addition to its fundamental interest, this remarkably high dichroism suggests a way of spatially resolving chiral optical excitations, including dark plasmons. We also predict a dichroic response when probing a chiral biomolecule, which suggests the use of these electron beams for resolving different enantiomers.

DOI: 10.1103/PhysRevLett.113.066102 PACS numbers: 68.37.Ma, 42.50.Tx, 73.20.Mf, 79.20.Uv

Vortex electron beams, which are known to exist as propagating solutions of the Schrödinger equation in free space [1], have been recently generated by passing electron beams through different types of phase masks [2–5] in order to select specific values of the orbital angular momentum (OAM). Following a previous suggestion [1,6], electron vortices have been additionally generated by exploiting the interaction between an electron beam and an effective magnetic monopole [7]. These advances have stimulated innovative ways of using electron beams to interact with nanostructured materials. For instance, electron vortices possess a magnetic moment proportional to the OAM that can make them excellent probes of core-level magnetic transitions. Recently, many works have analyzed the range of applicability of these vortices for performing magnetic chiral dichroism [8–10]. A similar effect has been proposed for mapping plasmons in nanostructures [11]. Additionally, the interaction with a longitudinal magnetic field has been predicted to produce Faraday rotation on the electron vortex [12]. This configuration has been also proposed as a way to observe the Aharonov-Bohm effect [13]. Chiral electron beams have even been postulated as suitable tools for inducing and controlling mechanical rotation of nanoparticles [14,15].

Electron vortex beams can be equally used to characterize the optical response of chiral (mirror-symmetry-breaking) structures. Traditionally, circularly polarized light, which carries spin angular momentum, has been used to probe chiral samples, as they produce polarization-dependent absorption cross sections (i.e., circular dichroism [16,17]). However, OAM dichroism cannot be observed when probing with optical Laguerre-Gauss beams [18–22], clearly revealing that chiral light-matter coupling is exclusively mediated by the intrinsic angular momentum of light. In contrast, electrons can undergo chiral transfer of OAM [20].

In this Letter, we demonstrate the chiral exchange of OAM between vortex electron beams and two different kinds of chiral samples: plasmonic nanostructures and biomolecules. In particular, we predict large differences in the intensity of opposite OAM components of electrons that are inelastically scattered from chiral clusters formed by closely arranged silver nanospheres, both under broad and focused vortex beam illumination. The latter can be used to map plasmonic chiral modes with high spatial resolution. We also predict significant dichroism in the electron energy-loss signal produced by α-helix molecules.

Energy loss probability.—We intend to study the probability that an electron prepared in incident state i undergoes inelastic transitions to final states f, accompanied by a net transfer of OAM and energy to a chiral sample. The transition rate is given by [23]

$$\frac{d\Gamma_{fi}}{dt} = \int d\omega \frac{d\Gamma_{fi}(\omega)}{dt},$$

where

$$\frac{d\Gamma_{fi}(\omega)}{dt} = \frac{2\hbar e^2}{\omega^2 m_e^2} \int d^3\mathbf{r} d^3\mathbf{r}' \psi_f(\mathbf{r}) \psi_f^*(\mathbf{r}') \delta(\varepsilon_f - \varepsilon_i + \omega) \times [\nabla \psi_i^*(\mathbf{r})] \cdot \mathrm{Im}\{\mathcal{G}(\mathbf{r}, \mathbf{r}', \omega)\} \cdot [\nabla \psi_i(\mathbf{r}')], \quad (1)$$

is the spectrally resolved rate, $\hbar\varepsilon_i$ and $\hbar\varepsilon_f$ are the initial and final electron energies, and $\mathcal{G}(\mathbf{r}, \mathbf{r}', \omega)$ is the electromagnetic Green tensor, which contains the fully retarded response of the sample (see the Supplemental Material [24]). The wave functions of energetic beam electrons can be well described as [23]

$$\psi_{i,f}(\mathbf{r}) = \frac{1}{\sqrt{L}} e^{ip_{zi,f}z} \psi_{i,f\perp}(\mathbf{R}), \quad (2)$$

where we assume a plane wave behavior along the beam direction z, L is the quantization length along that direction, and the dependence on transversal coordinates $\mathbf{R} = (x, y)$ is separated in $\psi_{i,f\perp}(\mathbf{R})$. The low-kinetic energies associated with the latter allows us to approximate the frequency transfer by $\omega = \varepsilon_i - \varepsilon_f \approx q_z v$ (nonrecoil approximation), where $q_z = p_{zi} - p_{zf}$ is the wave vector transfer and v is the electron velocity ($v = 0.55c$ for the 100 keV electrons considered in this work). Using Eq. (2) in Eq. (1), summing over final longitudinal wave vectors p_{zf}, and dividing by the electron current v/L derived from ψ_i, we find the probability that an electron undergoes a transition between $\psi_{i\perp}$ and $\psi_{f\perp}$ transversal states to have the form (see the Supplemental Material [24])

$$\Gamma(\omega) = \frac{4e^2\omega^2}{\pi\hbar v^4\gamma^2}\sum_{f\perp}\mathrm{Im}\{\mathbf{N}^+ \cdot \mathbb{\alpha} \cdot \mathbf{N}\},$$

where $\gamma = 1/\sqrt{1-(v/c)^2}$, $\mathbb{\alpha}$ is a generalized polarizability matrix describing the response of the sample (see below), and $\mathbf{N}$ is an electromagnetic matrix element.

Chiral plasmonic cluster.—Electron beams are valuable tools to spectrally and spatially map nanoscale plasmons, the collective oscillations of conduction electrons in metals [29,30]. Here, we consider plasmons in chiral clusters formed by non-mirror-symmetric geometrical arrangements of metallic spherical nanoparticles [31,32]. Four spheres are the minimum required to produce a chiral cluster [33]. In particular, we focus on a staircase tetramer and its mirror image, along with a nonchiral planar trimer. For simplicity, the particles are assumed to be small enough as to describe them through a scalar electric polarizability $\alpha(\omega)$, which turns out to be a good approximation for the 30 nm silver spheres separated by 5 nm gaps that we study below (see Fig. S2 in the Supplemental Material [24]). Simultaneously, the particle size and spacings are large enough to allow us to describe them using local classical theory [34]. We obtain $\alpha(\omega)$ using a tabulated dielectric function for silver [35]. For such clusters, we have

$$\mathbb{\alpha} = \frac{\mathbf{1}}{\alpha^{-1} - \mathcal{G}_0},$$

where $\mathcal{G}^0_{jj'}$ describes the retarded interaction between particle dipoles at positions $\mathbf{r}_j$ and $\mathbf{r}_{j'}$, and we use matrix notation with indices running over the three Cartesian directions for each and all of the spheres. The electromagnetic matrix element associated with particle j is then (see the Supplemental Material [24])

$$\mathbf{N}_j = e^{iq_z z_j}\int d^2\mathbf{R}\,\psi^*_{f\perp}(\mathbf{R})\psi_{i\perp}(\mathbf{R}) \times\left[\frac{\mathbf{u}_j}{|\mathbf{u}_j|}K_1\left(\frac{q_z|\mathbf{u}_j|}{\gamma}\right) + \hat{\mathbf{z}}\frac{i}{\gamma}K_0\left(\frac{q_z|\mathbf{u}_j|}{\gamma}\right)\right],$$

where K_0 and K_1 are modified Bessel functions of the second kind and $\mathbf{u}_j = \mathbf{R} - \mathbf{R}_j$. In what follows, we present numerical results obtained by evaluating these expressions for either incident electron plane waves (uniform $\psi_{i\perp}$) or Gaussian beams ($\psi_{i\perp} \propto e^{-R^2/\Delta^2}$). We consider transitions to a vortex electron carrying a definite amount of OAM $\hbar m_f$ [i.e., $\psi_{f\perp} \propto e^{im_f\varphi}J_{m_f}(P_f R)$], characterized by an orbital momentum number m_f and transversal wave vector P_f (see the Supplemental Material [24] for further details).

Inspired by the concept of circular dichroism in optics, we define dichroism in electron energy-loss spectroscopy (EELS) as the difference in the loss probability of electron vortices with opposite OAM (e.g., $\pm\hbar$). We envision an experiment in which the orbital number m_f can be pre (post)-selected by means of an OAM analyzer placed before (after) the sample. Although the design and fabrication of OAM analyzers still pose a tremendous experimental challenge, excellent progress has been recently made in this direction [5,36–38]. For simplicity, we study incident beams without a net OAM interacting with chiral samples and resolved in OAM components by a post-selection analyzer, although the present work can be trivially extended to deal with pre-selection analyzers. In particular, we first consider a 100 keV plane-wave electron passing through a chiral sample and subsequently entering an OAM analyzer, which deflects different m_f components along different outgoing directions [see Fig. 1(a)]. Energy loss spectra are recorded for several m_f's through an angle-resolved spectrometer. In the Fourier plane, the transmitted $m_f = \pm 1$ signals display a characteristic annular pattern, in contrast to the more intense $m_f = 0$ disklike angular map.

We obtain the m_f-resolved loss cross section $\sigma_{m_f}(\omega)$ for the incident plane wave by multiplying the transition probability by the wave front area (see the Supplemental Material [24]). The spectrally resolved cross section exhibits complex features with several peaks, corresponding to the excitation of plasmons in the cluster [Fig. 1(b)]. The $m_f = \pm 1$ spectra show slightly different intensity for each of the spectral features. This prompts us to define the absolute and relative degrees of dichroism associated with the orbital number m_f as $\sigma_{m_f} - \sigma_{-m_f}$ and $(\sigma_{m_f} - \sigma_{-m_f})/(\sigma_{m_f} + \sigma_{-m_f})$, respectively. For the clusters under consideration, these quantities decrease with increasing m_f [see Fig. 1(b)].

We study the $m_f = 1$ dichroism produced by different clusters in Fig. 2. The relative electron dichroism reaches up to ~10%, which is remarkably high compared with typical values in its optical counterpart [16,17]. As expected, the effect changes sign upon mirror reflection of the sample, while a cluster formed by only three particles lying on a plane normal to the beam does not produce dichroism at all, as it is not seen as chiral by the electron [Figs. 2(a), 2(b)]. In contrast, a net dichroism effect is observed for the trimer by tilting it [Fig. 2(c)], so that the electron sees again a staircaselike structure along the direction of electron propagation. In optics, this

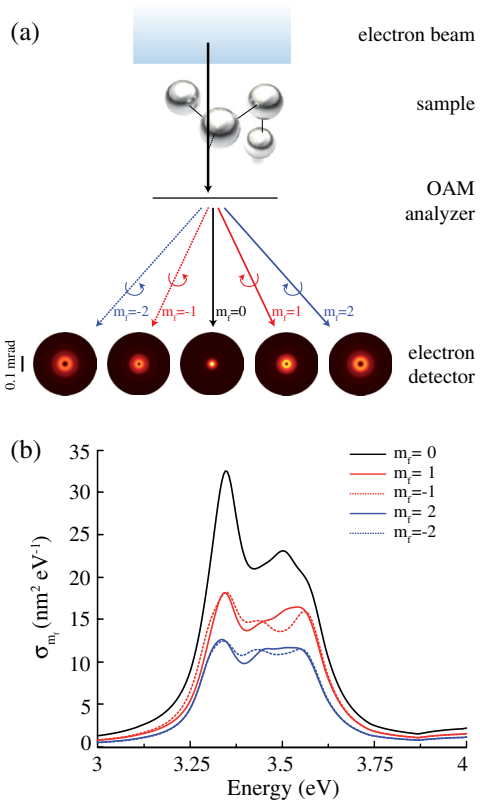

FIG. 1 (color online). (a) Sketch of the system under consideration. A 100 keV electron plane wave impinges on a cluster (left-handed tetramer) consisting of four 30 nm silver spheres separated by 5 nm gaps. The electron is subsequently passing through an orbital angular momentum (OAM) analyzer that splits the beam into different components m_f along different transmission directions. These components are independently energy-analyzed by an angle-resolved spectrometer. The origin of OAM is made to coincide with the position of the electron arrow depicted in (a). The angular distribution of different m_f components are represented at the bottom for a 3.5 eV energy loss. For visualization purposes, the intensities of the $m_f = \pm 1$ and $m_f = \pm 2$ components are multiplied by factors of 5 and 10, respectively. (b) Energy-loss m_f-resolved cross-section spectra under the conditions of (a).

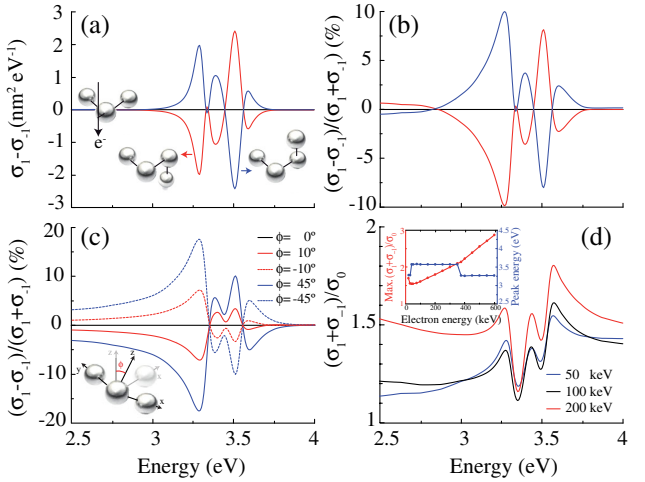

FIG. 2 (color online). (a) Dichroism between $m_f = \pm 1$ components in the spectrally resolved inelastic cross section of 100 keV electrons for different clusters of 30 nm silver spheres with gaps of 5 nm (see insets). The planar trimer does not exhibit any dichroism. (b) Same as (a), normalized to the sum of $m_f = \pm 1$ cross sections. (c) Extrinsic dichroism displayed by the trimer when it is tilted with respect to the direction of electron propagation. (d) Partial $m_f = \pm 1$ inelastic cross sections normalized to the $m_f = 0$ transmitted beam component for different electron energies in the left-handed tetramer [upper inset in (a)]. The inset of (d) shows the maximum of this ratio (left, red curve) and the energy loss at which this happens (right, blue curve) as a function of electron energy. The origin of OAM is the same as in Fig. 1

phenomenon is known as extrinsic dichroism, which is produced when oriented nonchiral molecules form a chiral triad with the light wave vector [39–41]. This is precisely what happens when the normal of the plane that contains the cluster is tilted with respect to the electron incidence direction, and once more, the effect changes sign upon mirror reflection of the sample. However, this apparent chirality is erased when averaging over all cluster orientations. It is important to stress that the fraction of inelastically scattered electrons that transfer OAM is actually large, as shown in Fig. 2(d) by comparing $m_f = \pm 1$ and $m_f = 0$ components.

Particle size and separation in the clusters play an important role in determining the strength of the chiral coupling to the electron (see Fig. S3 in the Supplemental Material [24]). Both the EELS intensity and the dichroism increase with particle size, but the latter is reduced with particle separation, as close interaction between the spheres is required to sustain a strong chiral plasmon that extends over the entire cluster.

The coupling to different chiral modes of the sample is also strongly affected by the relative position and alignment between the cluster and the vortex generator (see Fig. S3 in the Supplemental Material [24]). More precisely, the origin of electron OAM (i.e., the origin of azimuthal angles φ) depends on the design and position of the OAM analyzer. This poses an experimental challenge to measure the dichroic signal. If the planes of the sample and the OAM analyzer are taken to be conjugated in the electron optics setup, with a 1:100 demagnification factor for the analyzer, relative alignment requires sub-micron-scale displacements of the analyzer to produce nanometer-scale displacements at the conjugated sample plane.

Due to conservation of angular momentum, the OAM transferred by the electron produces a mechanical torque on the cluster, which can be separated into two different contributions: intrinsic torque acting on each individual particle and extrinsic torque acting on the cluster as a whole relative to the origin of electron OAM. Additionally, cathodoluminescence emission can take a net amount of angular momentum that needs to be included in this balance. As we show in the Supplemental Material [24],

neglecting retardation, the increase in angular momentum (intrinsic + extrinsic) produced by the self-consistent electromagnetic field resulting from interaction with the electron exactly accounts for the electron momentum transfer (see Fig. S4 in the Supplemental Material [24]).

The excellent spatial resolution of electron microscopes for visualizing optical near fields [23,42,43] can be used to study the chirality associated with each of the plasmon features. Remarkably, we find the relative degree of dichroism to display a sign and magnitude that are rather independent of the lateral width of the electron beam, although the absolute effect quickly vanishes for beams that are much narrower than the size of the plasmon modes (see Fig. S1 of the Supplemental Material [24]).

Chiral molecule.—Many biomolecules such as proteins and nucleic acids are chiral. Their optical response can be characterized by nonorthogonal electric (polar vector) and magnetic (axial vector) dipoles that, combined, break mirror symmetry [44]. In particular, the generalized polarizability of a chiral molecule contains electric (α_{EE}), magnetic (α_{MM}), and magnetoelectric ($\alpha_{\mathrm{ME}} = -\alpha_{\mathrm{EM}}^{T}$, due to reciprocity [45]) components that are combined in the matrix

$$\mathfrak{a} = \begin{bmatrix} \alpha_{\mathrm{EE}} & \alpha_{\mathrm{EM}} \\ \alpha_{\mathrm{ME}} & \alpha_{\mathrm{MM}} \end{bmatrix}.$$

Dichroism arises from the off-diagonal elements. The electromagnetic matrix element $\mathbf{N} = [\mathbf{N}_{\mathrm{EE}}, \mathbf{N}_{\mathrm{ME}}]$ also consists of two different components,

$$\mathbf{N}_{\mathrm{EE}} = \int d^2\mathbf{R}\psi^{*}_{f\perp}(\mathbf{R})\psi_{i\perp}(\mathbf{R}) \times \left[\frac{\mathbf{u}_0}{|\mathbf{u}_0|}K_1\left(\frac{q_z|\mathbf{u}_0|}{\gamma}\right) + \hat{\mathbf{z}}\frac{i}{\gamma}K_0\left(\frac{q_z|\mathbf{u}_0|}{\gamma}\right)\right],$$

$$\mathbf{N}_{\mathrm{ME}} = \frac{v}{c}\int d^2\mathbf{R}\psi^{*}_{f\perp}(\mathbf{R})\psi_{i\perp}(\mathbf{R})K_1\left(\frac{q_z|\mathbf{u}_0|}{\gamma}\right)\left(\hat{\mathbf{z}}\times\frac{\mathbf{u}_0}{|\mathbf{u}_0|}\right).$$

Remarkably, the ME crossed term is proportional to the ratio between the electron and light velocities, therefore suggesting that higher-energy electrons are better suited to study chiral molecules.

In Fig. 3 we study σ_1 (left panels) and the dichroism $|\sigma_1 - \sigma_{-1}|$ (right panels) as a function of energy loss for a model point structure (upper panels) and an α-helix molecule (lower panels). They are both considered to be randomly oriented and placed a distance R_0 apart from the origin of OAM. The model structure has a single chiral resonance of frequency ω_0, spectral width γ_0, and associated electric and magnetic dipole moments $\mathbf{p}$ and $\mathbf{m}$, respectively. The maxima of σ_1 and $|\sigma_1 - \sigma_{-1}|$ are normalized to yield the universal curves shown in Figs. 3(a), 3(b), which only depend on electron energy and $\omega_0 R_0/v\gamma$. These results can be applied to molecules and metamolecules [45] by simply plugging their corresponding spectral parameters. It is common to have $|\mathbf{m}| \ll |\mathbf{p}|$, so that the cross section is roughly proportional to $|\mathbf{p}|^2$, whereas the dichroism scales as $|\mathbf{m}\cdot\mathbf{p}|$. Interestingly,

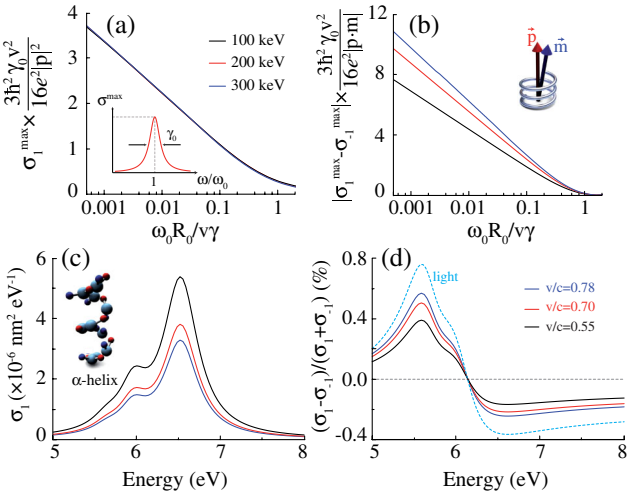

FIG. 3 (color online). (a),(b) Normalized maximum of the partial inelastic cross section σ_1 (a) and the dichroism $|\sigma_1 - \sigma_{-1}|$ (b) for a randomly oriented model point structure characterized by a chiral excitation of frequency ω_0, width γ_0, and associated electric and magnetic dipole moments $\mathbf{p}$ and $\mathbf{m}$ [see inset to (b)]. The cross section and dichroism spectra follow a Lorentzian profile [see inset to (a)]. The origin of OAM is displaced a distance R_0 with respect to the structure. The vertical axes are normalized to yield universal curves that only depend on the electron energy (see legend) and $\omega_0 R_0/v\gamma$. (c),(d) Partial inelastic cross section (c) and normalized dichroism (d) for an α-helix, parametrized as described in the Supplemental Material [24]). The optical dichroism with circularly polarized light is shown for reference. Different electron energies are considered with the same color code throughout the figure.

the absolute dichroism diverges logarithmically with decreasing R_0, thus suggesting a possible approach towards ultrasensitive detection of chirality consisting in lowering R_0 by employing a highly demagnified OAM analyzer.

Results for the α-helix biomolecule—a common secondary structure of proteins—are presented in Figs. 3(c), 3(d) using fitted parameters to model its three main UV resonances (see the Supplemental Material [24]) and taking $R_0 = 1$ nm. The universal curves obtained for the model structure provide a reasonable description of the spectra associated with each of these resonances. Interestingly, the calculated dichroism has a similar magnitude and profile as the optical dichroism that is obtained by replacing $\sigma_{\pm 1}$ by the extinction cross section of right (+1) and left (−1) circularly polarized light [Fig. 3(d)]. In practice, electron dichroism could be measured in molecular ensembles, which we predict to produce loss intensities comparable with those measured for nanoparticle plasmons [23] when the electrons are passing ∼1 nm apart from a few tens of molecules.

Concluding remarks.—We predict large transfers of orbital angular momentum and a remarkably high degree of dichroism in the inelastic interaction of electron beams with chiral structures. Unlike light, electrons can engage in dichroic transfer of orbital angular momentum, which provides an extra tool for probing intrinsic and extrinsic

rotational degrees of freedom. Combined with the spatial resolution of electron microscopes, this can be used to map different chiral modes in plasmonic structures, which are important elements of chiral metamaterials. The dichroism signal changes sign when mirror imaging the sample, and it disappears in systems that have mirror symmetry with respect to a plane perpendicular to the beam direction. The strength of the absolute dichroism is strongly dependent on the degree of focusing of the electron beam, and it is maximized when the beam size is comparable to the extension of the probed chiral mode. We also demonstrate that electron vortex beams can resolve the handedness of chiral biomolecules, which has great potential for biological and pharmaceutical studies.

We thank Johan Verbeeck and Giulio Guzzinati for helpful discussions and for a critical revision of the Letter. A. A.-G. acknowledges support through FPU from MEC.

*javier.garciadeabajo@icfo.es

[1] K. Y. Bliokh, Y. P. Bliokh, S. Savel'ev, and F. Nori, Phys. Rev. Lett. **99**, 190404 (2007).
[2] M. Uchida and A. Tonomura, Nature (London) **464**, 737 (2010).
[3] J. Verbeeck, H. Tian, and P. Schattschneider, Nature (London) **467**, 301 (2010).
[4] B. J. McMorran, A. Agrawal, I. M. Anderson, A. A. Herzing, H. J. Lezec, J. J. McClelland, and J. Unguris, Science **331**, 192 (2011).
[5] K. Saitoh, Y. Hasegawa, K. Hirakawa, N. Tanaka, and M. Uchida, Phys. Rev. Lett. **111**, 074801 (2013).
[6] T. T. Wu and C. N. Yang, Nucl. Phys. **B107**, 365 (1976).
[7] A. Béché, R. Van Boxem, G. Van Tendeloo, and J. Verbeeck, Nat. Phys. **10**, 26 (2014).
[8] S. M. Lloyd, M. Babiker, and J. Yuan, Phys. Rev. Lett. **108**, 074802 (2012).
[9] P. Schattschneider, S. Löffler, M. Stöger-Pollach, and J. Verbeeck, Ultramicroscopy **136**, 81 (2014).
[10] J. Rusz and S. Bhowmick, Phys. Rev. Lett. **111**, 105504 (2013).
[11] Z. Mohammadi, C. P. Van Vlack, S. Hughes, J. Bornemann, and R. Gordon, Opt. Express **20**, 15024 (2012).
[12] C. Greenshields, R. L. Stamps, and S. Franke-Arnold, New J. Phys. **14**, 103040 (2012).
[13] K. Y. Bliokh, P. Schattschneider, J. Verbeeck, and F. Nori, Phys. Rev. X **2**, 041011 (2012).
[14] J. Verbeeck, H. Tian, and G. V. Tendeloo, Adv. Mater. **25**, 1114 (2013).
[15] S. M. Lloyd, M. Babiker, and J. Yuan, Phys. Rev. A **88**, 031802 (2013).
[16] *Molecular Light Scattering and Optical Activity*, edited by L. D. Barron (Wiley, New York, 2004).
[17] D. B. Amabilino, *Chirality at the Nanoscale* (Wiley, New York, 2009).
[18] D. L. Andrews, L. C. Dávila Romero, and M. Babiker, Opt. Commun. **237**, 133 (2004).
[19] M. M. Coles and D. L. Andrews, Phys. Rev. A **85**, 063810 (2012).
[20] S. M. Lloyd, M. Babiker, and J. Yuan, Phys. Rev. A **86**, 023816 (2012).
[21] F. Araoka, T. Verbiest, K. Clays, and A. Persoons, Phys. Rev. A **71**, 055401 (2005).
[22] W. Löffler, D. J. Broer, and J. P. Woerdman, Phys. Rev. A **83**, 065801 (2011).
[23] F. J. García de Abajo, Rev. Mod. Phys. **82**, 209 (2010).
[24] See the Supplemental Material, which includes Refs. [25–28], at http://link.aps.org/supplemental/10.1103/PhysRevLett.113.066102, where we provide detailed derivations of all equations and formalism used in this paper, including expressions for the inelastic electron transition probability, the polarizability of spherical particles and chiral molecules, the Green tensor of a sphere cluster, and a parametrization of the absorption bands of the α-helix. We also include studies of the dependence of electron dichroism on relevant beam and sample parameters, the effect of sphere multipoles, and the conservation of linear and angular momentum during electron-sample interaction.
[25] F. J. García de Abajo, Phys. Rev. B **60**, 6086 (1999).
[26] B. T. Draine and P. J. Flatau, J. Opt. Soc. Am. A **11**, 1491 (1994).
[27] A. O. Govorov, Z. F. P. Hernandez, J. M. Slocik, and R. R. Naik, Nano Lett. **10**, 1374 (2010).
[28] W. C. Johnson and I. Tinoco, J. Am. Chem. Soc. **94**, 4389 (1972).
[29] H. Raether, *Surface Plasmons on Smooth and Rough Surfaces and on Gratings*, Springer Tracks in Modern Physics Vol. 11 (Springer-Verlag, Berlin, 1988).
[30] C. J. Powell and J. B. Swan, Phys. Rev. **115**, 869 (1959).
[31] J. K. Gansel, M. Thiel, M. S. Rill, M. Decker, K. Bade, V. Saile, G. von Freymann, S. Linden, and M. Wegener, Science **325**, 1513 (2009).
[32] A. Kuzyk, R. Schreiber, Z. Fan, G. Pardatscher, E.-M. Roller, A. Högele, F. C. Simmel, A. O. Govorov, and T. Liedl, Nature (London) **483**, 311 (2012).
[33] X. Shen, A. Asenjo-Garcia, Q. Liu, Q. Jiang, F. J. García de Abajo, N. Liu, and B. Ding, Nano Lett. **13**, 2128 (2013).
[34] J. Zuloaga, E. Prodan, and P. Nordlander, Nano Lett. **9**, 887 (2009).
[35] P. B. Johnson and R. W. Christy, Phys. Rev. B **6**, 4370 (1972).
[36] T. S. Yahn, J. S. Pierce, T. R. Harvey, and B. J. McMorran, Microsc. Microanal. **19**, Suppl. 2, 1166 (2013).
[37] G. Guzzinati, L. Clark, A. Béché, and J. Verbeeck, Phys. Rev. A **89**, 025803 (2014).
[38] L. Clarck, A. Béché, G. Guzzinati, and J. Verbeeck, Phys. Rev. A **89**, 053818 (2014).
[39] C. W. Bunn, *Chemical Crystallography* (Oxford University, New York, 1945).
[40] R. Williams, Phys. Rev. Lett. **21**, 342 (1968).
[41] E. Plum, X.-X. Liu, V. A. Fedotov, Y. Chen, D. P. Tsai, and N. I. Zheludev, Phys. Rev. Lett. **102**, 113902 (2009).
[42] J. Nelayah, M. Kociak, O. Stéphan, F. J. García de Abajo, M. Tencé, L. Henrard, D. Taverna, I. Pastoriza-Santos, L. M. Liz-Marzán, and C. Colliex, Nat. Phys. **3**, 348 (2007).
[43] D. Rossouw, M. Couillard, J. Vickery, E. Kumacheva, and G. A. Botton, Nano Lett. **11**, 1499 (2011).
[44] N. Berova, K. Nakanishi, and R. W. Woody, *Circular Dichroism: Principles and Applications* (VCH, New York, 1994).
[45] I. Sersic, C. Tuambilangana, T. Kampfrath, and A. F. Koenderink, Phys. Rev. B **83**, 245102 (2011).

Supplemental Material for "Dichroism in the Interaction between Vortex Electron Beams, Plasmons, and Molecules"

A. Asenjo-Garcia[1] and F. J. García de Abajo[1,2,*]

[1] *ICFO - Institut de Ciencies Fotoniques, Mediterranean Technology Park, 08860 Castelldefels (Barcelona), Spain*
[2] *ICREA-Institució Catalana de Recerca i Estudis Avançats, Passeig Lluís Companys, 23, 08010 Barcelona, Spain*

(Dated: July 14, 2014)

We derive retarded and non-retarded expressions for the spectrally resolved probability that a beam electron undergoes inelastic transitions between two different transversal wave-function states upon interaction with either a cluster of small particles or a chiral molecule. Semi-analytical equations are obtained for both extended plane-wave and focused Gaussian-beam electrons when the final state is resolved in orbital angular momentum components. We offer details on the optical response of clusters formed by small spheres, along with additional numerical results that supplement those of the main paper. We further show that the change in linear and angular momentum experienced by the electron is transformed into mechanical motion of the cluster, assuming a negligible momentum transfer to emitted radiation. The momentum-resolved energy loss due to a chiral molecule is also calculated from its polarizability, which we express in terms of effective electric and magnetic dipole matrix elements.

Contents

*Electronic address: javier.garciadeabajo@icfo.es

I. CHIRAL ARRANGEMENT OF A CLUSTER OF NANOPARTICLES

A. Inelastic electron transition probability

The rate at which a beam electron undergoes transitions from an initial state i to final states f is given by [1]

$$\frac{d\Gamma_{fi}}{dt} = \int_0^\infty d\omega \, \frac{d\Gamma_{fi}(\omega)}{dt},$$

where

$$\frac{d\Gamma_{fi}(\omega)}{dt} = \frac{2\hbar e^2}{\omega^2 m_e^2} \int d^3\mathbf{r}\, d^3\mathbf{r}' \psi_f(\mathbf{r}) \psi_f^*(\mathbf{r}') [\nabla \psi_i^*(\mathbf{r})] \cdot \mathrm{Im}\{\mathcal{G}(\mathbf{r}, \mathbf{r}', \omega)\} \cdot [\nabla \psi_i(\mathbf{r}')] \, \delta(\varepsilon_f - \varepsilon_i + \omega) \tag{1}$$

is the spectrally resolved rate, which is a function of energy loss $\hbar\omega$. The coupling to the sample is mediated by the electromagnetic 3×3 Green tensor $\mathcal{G}$ (see Appendix B). Beam electrons can be well described using plane waves along the direction of the beam z, with the electron wave functions decomposed as

$$\psi(\mathbf{r}) = \frac{1}{\sqrt{L}} \mathrm{e}^{\mathrm{i}p_z z} \psi_\perp(\mathbf{R}),$$

where L is the quantization length along z, whereas $\psi_\perp(\mathbf{R})$ contains the dependence on the transversal plane coordinates $\mathbf{R} = (x, y)$. In what follows, we consider beams of small divergence angle, so that the transversal momentum components $\mathbf{P}$ associated with $\psi_\perp$ are small compared with p_z (i.e., $|p_z| \gg |\mathbf{P}|$).

We sum over final plane wave states and separate this sum into longitudinal and transversal components as

$$\sum_f \to \frac{L}{2\pi} \int dp_{zf} \sum_{f_\perp}.$$

The p_{zf} integral can be carried out using the δ function of Eq. (1), involving the expression

$$\int dp_{zf} \, \mathrm{e}^{\mathrm{i}(p_{zf} - p_{zi})(z - z')} \delta(\varepsilon_f - \varepsilon_i + \omega) = \frac{1}{v} \mathrm{e}^{-\mathrm{i}q_z(z - z')},$$

where

$$q_z = p_{zi} - p_{zf} = \omega / v$$

and we have neglected electron recoil [1] [i.e., the transferred frequency is approximated as $(\varepsilon_f - \varepsilon_i) \approx (p_{zf} - p_{zi})v$]. We further neglect the gradient of the electron wave function along the transversal direction and divide by the electron beam current v/L in order to obtain the probability per electron. We find

$$\Gamma(\omega) = \sum_{f_\perp} \int d^2\mathbf{R}\, d^2\mathbf{R}' \, \psi_{f\perp}(\mathbf{R}) \psi_{i\perp}^*(\mathbf{R}) \psi_{f\perp}^*(\mathbf{R}') \psi_{i\perp}(\mathbf{R}') \, h(\mathbf{R}, \mathbf{R}', \omega), \tag{2}$$

where

$$h(\mathbf{R}, \mathbf{R}', \omega) = \frac{e^2}{\pi\hbar\omega^2} \int dz\, dz' \, \mathrm{e}^{-\mathrm{i}q_z(z - z')} \, \mathrm{Im}\big\{\mathcal{G}_{zz}(\mathbf{r}, \mathbf{r}', \omega)\big\}, \tag{3}$$

and we have dropped the initial-state subindex i for simplicity. From here, using the expression for the Green tensor of a cluster of small spheres derived in Appendix B [Eq. (B7)], we obtain

$$h(\mathbf{R}, \mathbf{R}', \omega) = \frac{e^2}{\pi\hbar\omega^2} \int dz\, dz' \, \mathrm{e}^{-\mathrm{i}q_z(z - z')} \sum_{j,j'} \mathrm{Im} \left\{ \big[\hat{\mathbf{z}} \cdot \mathcal{G}^0(\mathbf{r} - \mathbf{r}_j, \omega)\big] \cdot \left(\frac{\mathbf{1}}{\alpha^{-1} - \mathcal{G}^0} \right)_{jj'} \cdot \big[\hat{\mathbf{z}} \cdot \mathcal{G}^0(\mathbf{r}' - \mathbf{r}_{j'}, \omega)\big] \right\},$$

where $\mathcal{G}^0(\mathbf{r}, \omega)$ is given by Eq. (B3) and $\mathcal{G}^0_{jj'} = \mathcal{G}^0(\mathbf{r}_j - \mathbf{r}_{j'}, \omega)$. The evaluation of the z and z' integrals in the above expression involves

$$\begin{aligned} \int dz \, \mathrm{e}^{\mathrm{i}q_z z} \, \hat{\mathbf{z}} \cdot \mathcal{G}^0(\mathbf{r} - \mathbf{r}_j, \omega) &= 2 \left(\frac{\omega^2}{c^2} \hat{\mathbf{z}} + \nabla_j \partial_{z_j} \right) \mathrm{e}^{\mathrm{i}q_z z_j} K_0 \left(\frac{q_z |\mathbf{R} - \mathbf{R}_j|}{\gamma} \right) \\ &= 2\mathrm{i} \frac{q_z^2}{\gamma} \mathrm{e}^{\mathrm{i}q_z z_j} \left[\frac{(\mathbf{R} - \mathbf{R}_j)}{|\mathbf{R} - \mathbf{R}_j|} K_1 \left(\frac{q_z |\mathbf{R} - \mathbf{R}_j|}{\gamma} \right) + \hat{\mathbf{z}} \frac{i}{\gamma} K_0 \left(\frac{q_z |\mathbf{R} - \mathbf{R}_j|}{\gamma} \right) \right], \end{aligned}$$

where $\gamma = 1/\sqrt{1-(v/c)^2}$. Finally, the probability for the electron to undergo a transition between the initial and final transversal states $\psi_{i\perp}$ and $\psi_{f\perp}$ reduces to

$$\Gamma(\omega) = \frac{4e^2 q_z^2}{\pi\hbar v^2\gamma^2}\sum_{f_\perp}\mathrm{Im}\{\mathbf{N}^+\cdot\frac{\mathbf{1}}{\alpha^{-1}-\mathcal{G}^0}\cdot\mathbf{N}\}, \tag{4}$$

where the components of the vector $\mathbf{N}$, which are labeled by the three Cartesian directions for each and all of the spheres j, are given by

$$\mathbf{N}_j = \mathrm{e}^{\mathrm{i}q_z z_j}\int d^2\mathbf{R}\;\psi^*_{f\perp}(\mathbf{R})\psi_{i\perp}(\mathbf{R})\;\left[\frac{(\mathbf{R}-\mathbf{R}_j)}{|\mathbf{R}-\mathbf{R}_j|}K_1\left(\frac{q_z|\mathbf{R}-\mathbf{R}_j|}{\gamma}\right)+\hat{\mathbf{z}}\frac{i}{\gamma}K_0\left(\frac{q_z|\mathbf{R}-\mathbf{R}_j|}{\gamma}\right)\right].$$

Notice that $\mathcal{G}^0$ is a $3n\times 3n$ matrix for a cluster consisting of n particles, whereas $\mathbf{N}$ has dimension $3n\times 1$.

1. *Transitions from a plane-wave to a vortex*

For an electron plane wave propagating along the direction z, we can write the initial transversal wave function as

$$\psi_{i\perp}(\mathbf{R}) = \frac{1}{\sqrt{A}},$$

where A is the quantization area in the x-y transversal plane. We now consider a complete orthonormal basis set of transversal plane waves labeled by wave vectors $\mathbf{P}_f$, which can be decomposed as

$$\psi_{f\perp}(\mathbf{R}) = \frac{1}{\sqrt{A}}\mathrm{e}^{\mathrm{i}\mathbf{P}_f\cdot\mathbf{R}} = \frac{1}{\sqrt{A}}\sum_{m_f=-\infty}^{\infty}\mathrm{i}^{m_f}\mathrm{e}^{\mathrm{i}m_f(\varphi-\varphi_{\mathbf{P}_f})}J_{m_f}(P_f R)$$

in terms of Bessel functions J_m, using polar coordinates $\mathbf{R}=(R,\varphi)$ and $\mathbf{P}_f=(P_f,\varphi_{\mathbf{P}_f})$. As we are only interested in transitions to a given component of final angular momentum m_f, it is convenient to use the complete set of final states

$$\psi_{f\perp}(\mathbf{R}) = \frac{1}{\sqrt{A}}\mathrm{i}^{m_f}\mathrm{e}^{\mathrm{i}m_f\varphi}J_{m_f}(P_f R), \tag{5}$$

in which each state is characterized by a particular choice of P_f and m_f. With this final state representation, the components of vector $\mathbf{N}$ become

$$\mathbf{N}_j = \frac{(-\mathrm{i})^{m_f}}{A}\mathrm{e}^{\mathrm{i}q_z z_j}\int d^2\mathbf{R}\;\mathrm{e}^{-\mathrm{i}m_f\varphi}J_{m_f}(P_f R)\;\left[\frac{(\mathbf{R}-\mathbf{R}_j)}{|\mathbf{R}-\mathbf{R}_j|}K_1\left(\frac{q_z|\mathbf{R}-\mathbf{R}_j|}{\gamma}\right)+\hat{\mathbf{z}}\frac{i}{\gamma}K_0\left(\frac{q_z|\mathbf{R}-\mathbf{R}_j|}{\gamma}\right)\right].$$

The angular integral of the z component of this vector reduces to

$$\int d\varphi\,\mathrm{e}^{-\mathrm{i}m_f\varphi}K_0\left(\frac{q_z|\mathbf{R}-\mathbf{R}_j|}{\gamma}\right) = 2\pi\,\mathrm{e}^{-\mathrm{i}m_f\varphi_j}I_{m_f}\left(\frac{q_z R_<}{\gamma}\right)K_{m_f}\left(\frac{q_z R_>}{\gamma}\right),$$

where $R_< = \min\{R,R_j\}$, $R_> = \max\{R,R_j\}$, and I_m and K_m are modified Bessel functions. Likewise, the remaining transversal components involve

$$\begin{aligned}
&\int d\varphi\,\mathrm{e}^{-\mathrm{i}m_f\varphi}\frac{(\mathbf{R}-\mathbf{R}_j)}{|\mathbf{R}-\mathbf{R}_j|}K_1\left(\frac{q_z|\mathbf{R}-\mathbf{R}_j|}{\gamma}\right)\\
&= 2\pi\mathrm{e}^{-\mathrm{i}m_f\varphi_j}\times\begin{cases} I_{m_f}\left(\frac{q_z R}{\gamma}\right)K'_{m_f}\left(\frac{q_z R_j}{\gamma}\right)\hat{\mathbf{R}}_j-\mathrm{i}m_f\frac{\gamma}{q_z R_j}I_{m_f}\left(\frac{q_z R}{\gamma}\right)K_{m_f}\left(\frac{q_z R_j}{\gamma}\right)\hat{\varphi}_j, & (R\le R_j)\\ K_{m_f}\left(\frac{q_z R}{\gamma}\right)I'_{m_f}\left(\frac{q_z R_j}{\gamma}\right)\hat{\mathbf{R}}_j-\mathrm{i}m_f\frac{\gamma}{q_z R_j}K_{m_f}\left(\frac{q_z R}{\gamma}\right)I_{m_f}\left(\frac{q_z R_j}{\gamma}\right)\hat{\varphi}_j, & (R>R_j)\end{cases}
\end{aligned}$$

where (R_j,φ_j) are the polar coordinates of $\mathbf{R}_j$. For the incident plane wave under consideration, it is useful to define the loss cross-section, which we separate in different transferred frequency components as

$$\sigma_{m_f} = \int_0^\infty d\omega\;\sigma_{m_f}(\omega).$$

We obtain the cross section as the transition probability per electron multiplied by the transversal area A, that is, $\sigma_{m_f}(\omega) = A\Gamma(\omega)$. A more convenient expression is derived by summing over final transversal wave vectors $\mathbf{P}_f$ using the customary prescription

$$\sum_{f_\perp} \to \frac{A}{(2\pi)^2}\int_0^\infty P_f dP_f \int_0^{2\pi} d\varphi_f = \frac{A}{2\pi}\int_0^\infty P_f dP_f,$$

which leads to

$$\sigma_{m_f}(\omega) = \frac{8e^2q_z^2}{\hbar v^2\gamma^2}\int_0^\infty P_f\, dP_f \mathrm{Im}\left\{\mathbf{M}^+\cdot\frac{\mathbf{1}}{\alpha^{-1}-\mathcal{G}^0}\cdot\mathbf{M}\right\}.$$

Here, the components of vector $\mathbf{M}$ are

$$\begin{aligned}\mathbf{M}_j &= \mathrm{e}^{\mathrm{i}q_z z_j}\mathrm{e}^{-\mathrm{i}m_f\varphi_j} \\ &\times\left\{\left[g_1\, K'_{m_f}\left(\frac{q_zR_j}{\gamma}\right)+g_2\, I'_{m_f}\left(\frac{q_zR_j}{\gamma}\right)\right]\hat{R}_j+\left[g_1\, K_{m_f}\left(\frac{q_zR_j}{\gamma}\right)+g_2\, I_{m_f}\left(\frac{q_zR_j}{\gamma}\right)\right]\mathrm{i}\left(\frac{-m_f\gamma}{R_jq_z}\hat{\varphi}_j+\frac{1}{\gamma}\hat{z}_j\right)\right\},\end{aligned} \tag{6}$$

and we have defined

$$\begin{aligned}g_1 &= \int_0^{R_j} R\,dR\, J_{m_f}(P_fR)\, I_{m_f}\left(\frac{q_zR}{\gamma}\right), \\ g_2 &= \int_{R_j}^\infty R\,dR\, J_{m_f}(P_fR)\, K_{m_f}\left(\frac{q_zR}{\gamma}\right).\end{aligned} \tag{7}$$

Finally, we decompose the cross section in transversal momentum components as

$$\sigma_{m_f}(\omega) = \int d^2\mathbf{P}_f\, \sigma_{m_f}(\mathbf{P}_f,\omega)$$

where

$$\sigma_{m_f}(\mathbf{P}_f,\omega) = \frac{4e^2q_z^2}{\pi\hbar v^2\gamma^2}\mathrm{Im}\left\{\mathbf{M}^+\cdot\frac{\mathbf{1}}{\alpha^{-1}-\mathcal{G}^0}\cdot\mathbf{M}\right\}.$$

Further analysis and results of this section are presented in the main paper.

2. Transitions from a focused Gaussian beam to a vortex

A transversally focused beam is well represented by a Gaussian wave function

$$\psi_{i\perp}(\mathbf{R}) = \frac{1}{\sqrt{\pi}\Delta}\mathrm{e}^{-R^2/\Delta^2}.$$

We consider again the final vortex states of Eq. (5) and concentrate on a specific final angular momentum number m_f. Following the same procedure as in Sec. I A 1, we find that the loss probability reduces to

$$\Gamma_{m_f}(\omega) = \frac{8e^2q_z^2}{\pi\hbar\Delta^2v^2\gamma^2}\int_0^\infty P_f\, dP_f \mathrm{Im}\left\{\mathbf{M}^+\cdot\frac{\mathbf{1}}{\alpha^{-1}-\mathcal{G}^0}\cdot\mathbf{M}\right\}, \tag{8}$$

where the vector $\mathbf{M}$ is still given by Eq. (6) with an appropriate redefinition of the functions

$$\begin{aligned}g_1 &= \int_0^{R_j} R\,dR\, J_{m_f}(P_fR)\, I_{m_f}\left(\frac{q_zR}{\gamma}\right)\,\mathrm{e}^{-R^2/\Delta^2}, \\ g_2 &= \int_{R_j}^\infty R\,dR\, J_{m_f}(P_fR)\, K_{m_f}\left(\frac{q_zR}{\gamma}\right)\,\mathrm{e}^{-R^2/\Delta^2}.\end{aligned}$$

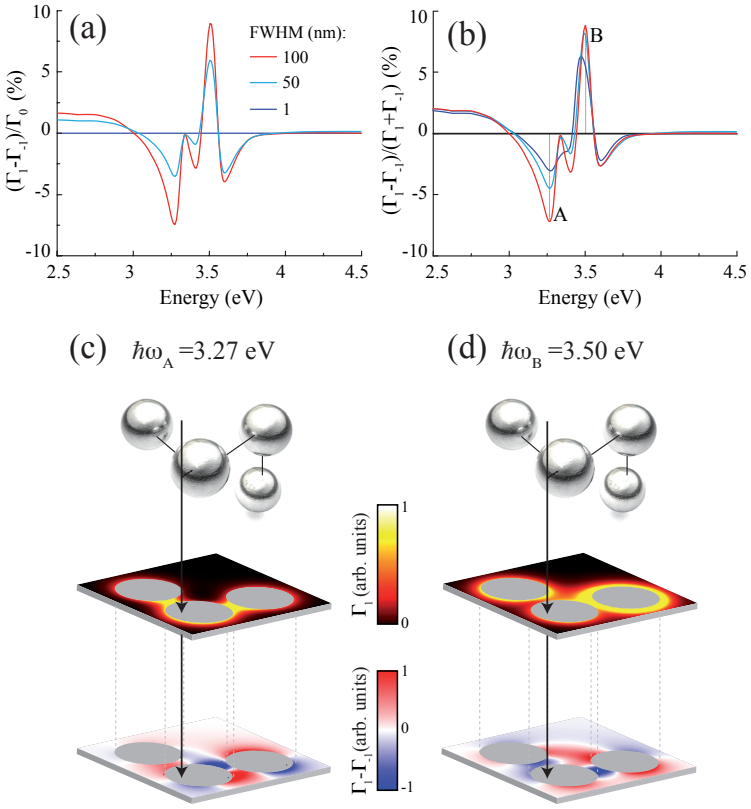

FIG. S1: Dichroism for a focused electron beam. **(a,b)** Absolute (a) and relative (b) degrees of dichroism for Gaussian beams of $\exp(-R^2/\Delta^2)$ profile with different values of the FWHM$= 2\sqrt{\ln 2}\Delta \approx 1.4\,\Delta$. The position and orientation of the beam relative to the sample is shown in the inset of (c). The origin of orbital angular momentum (OAM) is made to coincide with the center of the electron beam. **(c,d)** Energy loss probability (upper density plots) and dichroism (lower plots) distributions as a function of beam position for FWHM$=1$ nm and two different loss energies, corresponding to features A and B in (b). The electron energy is 100 keV. The cluster is made of 30 nm silver spheres separated by 5 nm gaps.

Finally, the wave-vector resolved probability, defined through

$$\Gamma_{m_f}(\omega) = \int d^2\mathbf{P}_f \, \Gamma_{m_f}(\mathbf{P}_f, \omega),$$

reads

$$\Gamma_{m_f}(\mathbf{P}_f, \omega) = \frac{4e^2 q_z^2}{\pi^2 \hbar \Delta^2 v^2 \gamma^2} \mathrm{Im}\left\{ \mathbf{M}^+ \cdot \frac{\mathbf{1}}{\alpha^{-1} - \mathcal{G}^0} \cdot \mathbf{M} \right\}.$$

By analogy to the definitions of the main paper, where we use the cross section, we now define the degree of dichroism with focused beams using the probability given by Eq. (8). We show some calculated spectra for incident Gaussian beams of different full width at half maximum (FWHM) and $m_f = 1$ in Fig. S1(a,b). Selected maps of the EELS intensity (upper plots) and the dichroism (lower plots) as a function of beam position reveal that both of these quantities are enhanced at the particle gaps [Fig. S1(c,d)]. However, the dichroic signal is more delocalized and changes sign when moving from the gaps to other neighboring regions of the cluster. The net orbital angular momentum transfer is thus rather sensitive to the position of the beam relative to the sample.

B. Multipolar versus dipolar response

The validity of the dipolar approximation used here to describe the particles can be questionable when multipolar contributions become important at short separations. We show that the dipolar approximation is qualitatively

correct by examining light extinction cross-sections and circular dichroism spectra, for which we perform converged electromagnetic simulations with full inclusion of all multiples up to a high order using a multiple elastic scattering of multipolar expansions (MESME) approach [2]. In particular, considering 30 nm silver spheres, Fig. S2 shows that for surface-to-surface distances as small as 5 nm (black curves) the agreement between multipolar and dipolar calculations is qualitatively reasonable and becomes quantitatively good for separations of 10 nm (red cuves).

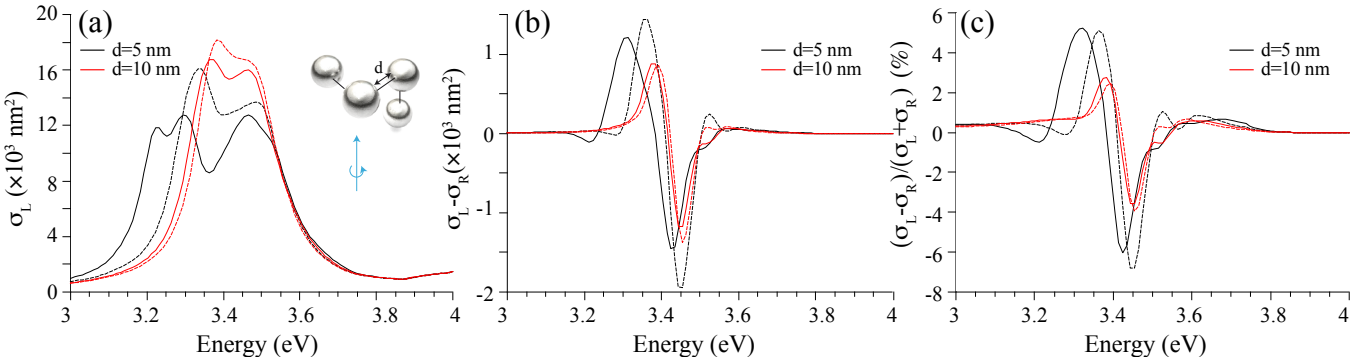

FIG. S2: Left circularly polarized light extinction cross-section (a), dichroism (b), and normalized dichroism (c) as a function of photon enegy for the cluster shown in the inset of (a) and two different surface-to-surface distances d. Light propagates along the direction of the blue arrow. Continuous (broken) curves correspond to multipolar (dipolar) calculations. The clusters consist of 30 nm silver spheres.

C. Influence of relevant parameters on electron dichroism

We present additional results showing the dependence of the dichroic signal on various parameters for an extended plane-wave electron interacting with a staircase tetramer arrangement of nanospheres [see inset of Fig. S3(a)]. In particular, the dependence on the material, particle radius, and separation between particles is analyzed in Fig. S3(a)-(c). The dichroism for silver spheres is considerably large compared with gold particles [Fig. S3(a)] because silver is a less lossy material. Additionally, the dichroism exhibits a steep increase in magnitude with particle size [Fig. S3(b)], and a decrease with particle separation [Fig. S3(c)], in agreement with the intuitive idea that larger structures can transfer a bigger amount of angular momentum, provided the coupling between spheres is sufficiently strong. We discuss the effect of the position of the orbital angular momentum (OAM) analyzer relative to the sample in Fig. S3(d). In these calculations, the electron beam is centered at the origin of OAM. This center is essentially determining where the origin of 2D angular momentum has to be taken [i.e., the point with respect to which the azimuthal angle φ is measured when specifying a given orbital angular number m associated with an $\exp(im\varphi)$ electron wave function dependence]. The planes of the sample and the analyzer are taken to be conjugated in the electron optics setup, although the analyzer is generally demagnified in actual experiments, so that sample/analyzer alignment requires sub-micron-scale displacements of the analyzer corresponding to nanometer-scale displacements at the conjugated sample plane.

D. Mode decomposition in the non-retarded limit

In the non-retarded limit, Eq. (1) reduces to [1]

$$\frac{d\Gamma(\omega)}{dt} = \frac{2e^2}{\hbar}\sum_f \int d^3\mathbf{r}\, d^3\mathbf{r}'\, \psi_f(\mathbf{r})\psi_i^*(\mathbf{r})\psi_f^*(\mathbf{r}')\psi_i(\mathbf{r}')\, \mathrm{Im}\big\{-W^{\mathrm{ind}}(\mathbf{r},\mathbf{r}',\omega)\big\}\,\delta(\varepsilon_f-\varepsilon_i+\omega),$$

where the coupling to the sample is mediated by the induced screened interaction W^{ind}. Working in frequency space ω, the electrostatic screened interaction $W(\mathbf{r},\mathbf{r}',\omega)$ is defined as the electric potential produced at $\mathbf{r}$ by an external point charge at $\mathbf{r}'$, and for a cluster consisting on n particles, it is given by

$$W^{\mathrm{ind}}(\mathbf{r},\mathbf{r}',\omega) = -\mathbf{T}(\mathbf{r})^{+}\cdot\frac{\mathbf{1}}{\alpha^{-1}(\omega)-\mathcal{G}^0}\cdot\mathbf{T}(\mathbf{r}'), \tag{9}$$

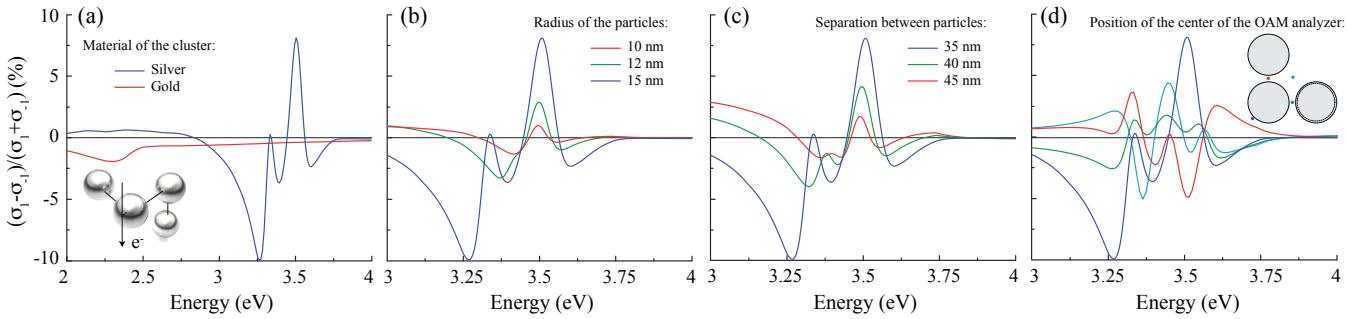

FIG. S3: **(a-c)** Influence of cluster material (a), particle size (b), and separation between particles (c) on the dichroism produced on a plane-wave electron upon interation with a staircase chiral tetramer arrangement of spheres [see inset in (a)]. **(d)** Dichroism for different positions of the OAM analyzer relative to the tetramer. Each spectral curve corresponds to a different position of the analyzer center, as indicated by a dot of the same color in the inset. The following default parameters are assumed, unless otherwise specified (see legends): 100 keV electrons, 15 nm particle radius, and 35 nm center-to-center particle spacing. In (a-c) the analyzer is at the position of the electron arrow of the inset to (a), which corresponds to the dark blue dot of the inset to (d) (1 nm apart from the sphere surface, same as in Figs. 1 and 2 of the main paper).

where the components of the vector $\mathbf{T}$ run over the three Cartesian directions for each and all of the spheres j and are given by

$$\mathbf{T}_j(\mathbf{r}) = \frac{\mathbf{r}-\mathbf{r}_j}{|\mathbf{r}-\mathbf{r}_j|^3} = \nabla_j \frac{1}{|\mathbf{r}-\mathbf{r}_j|}.$$

Equation (9) can be derived in a similar way as its retarded counterpart (see Appendix B). Likewise, the non-retarded Green tensor $\mathcal{G}^0$ is given by the $k \to 0$ limit of Eq. (B3). As $\mathcal{G}^0$ is real and symmetric, its eigenvectors form an orthonormal basis set, each of them defining a mode of the system. The energy loss suffered by the electron can then be separated as the sum of the contributions from the resulting $3n$ modes. Using matrix notation

$$\mathcal{G}^0 \cdot \mathbf{p}_l = \mu_l \mathbf{p}_l,$$

where $\mathbf{p}_l$ and μ_l are the real eigenvector and eigenvalue of mode l, Eq. (9) can be recast into

$$W^{\rm ind}(\mathbf{r},\mathbf{r}',\omega) = -\sum_l \mathbf{T}(\mathbf{r})^+ \cdot \mathbf{p}_l \frac{\mathbf{1}}{\alpha^{-1}(\omega)-\mu_l} \mathbf{p}_l^+ \cdot \mathbf{T}(\mathbf{r}').$$

After some algebra, the loss probability reduces to

$$\Gamma(\omega) = \frac{e^2}{\pi\hbar v^2} \sum_l {\rm Im}\left\{\frac{\mathbf{1}}{\alpha^{-1}(\omega)-\mu_l}\right\} \sum_{f_\perp} |N_l|^2,$$

where

$$N_l = \int d^3\mathbf{r}\, {\rm e}^{{\rm i}q_z z} \psi^*_{f\perp}(\mathbf{R})\psi_{i\perp}(\mathbf{R})\, \mathbf{p}_l^+ \cdot \mathbf{T}(\mathbf{r}) = \frac{1}{\pi}\sum_j \mathbf{p}_{l,j} \cdot \nabla_j\, {\rm e}^{{\rm i}q_z z_j} \int d^2\mathbf{R} \int d^2\mathbf{Q}\, \frac{{\rm e}^{-{\rm i}\mathbf{Q}\cdot(\mathbf{R}-\mathbf{R}_j)}}{Q^2+q_z^2}\, \psi^*_{f\perp}(\mathbf{R})\psi_{i\perp}(\mathbf{R}).$$

Finally, for a transition from an incident plane wave to a m_f vortex beam, the inelastic cross-section reduces to

$$\sigma_{m_f}(\omega) = \frac{8e^2}{\hbar v^2} \sum_l {\rm Im}\left\{\frac{\mathbf{1}}{\alpha^{-1}(\omega)-\mu_l}\right\} \int_0^\infty \frac{P_f\, dP_f}{\left[P_f^2+q_z^2\right]^2} |M_l(P_f)|^2,$$

where

$$\begin{aligned} M_l(P_f) &= \sum_j \mathbf{p}_{l,j} \cdot \nabla_j \left[{\rm e}^{-{\rm i}m_f\varphi_j} {\rm e}^{{\rm i}q_z z_j} J_{m_f}(P_f R_j)\right] \\ &= \sum_j {\rm e}^{-{\rm i}m_f\varphi_j} {\rm e}^{{\rm i}q_z z_j} \left[P_f J'_{m_f}(P_f R_j)\mathbf{p}_{l,j}\cdot\hat{\mathbf{R}}_j - \frac{{\rm i}m_f}{R_j} J_{m_f}(P_f R_j)\mathbf{p}_{l,j}\cdot\hat{\varphi}_j + {\rm i}q_z\, J_{m_f}(P_f R_j)\mathbf{p}_{l,j}\cdot\hat{\mathbf{z}}_j\right]. \end{aligned}$$

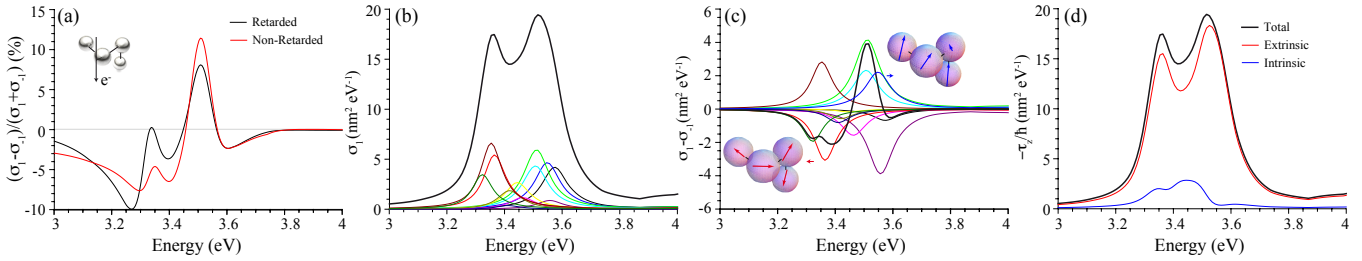

FIG. S4: **(a)** Retarded and non-retarded dichroism for the cluster shown in the inset. **(b,c)** Non-retarded calculation of the inelastic cross-section (b) and the dichroism (c). The black curve corresponds to the total result, while the contributions of individual plasmon modes are shown in different colors. The insets in (c) illustrate the dipole orientations for two of these modes. The incident electron is a 100 keV plane wave, while the cluster is made of 30 nm silver spheres separated by 5 nm gaps. **(d)** Total, extrinsic, and intrinsic z-component of the non-retarded torque, normalized to yield cross-section units. We consider transitions from the incident plane wave to a $m = 1$ vortex in all cases.

We compare retarded and non-retarded calculations in Fig. S4(a). Although we present retarded simulations in the main paper, the non-retarded theory is qualitatively correct, so we use it in next section to analyze the transfer of angular momentum to the sample. Incidentaly, many modes contribute to both the energy loss and the dichroism, thus resulting in a non-trivial dichroic signal that cannot be ascribed in general to specific dominant modes [see Fig. S4(b,c)].

E. Mechanical transfer of linear and angular momentum to the sample

The torque and force exerted by the electron on the cluster can be calculated from the Maxwell stress tensor [1]. We summarize the resulting expressions when applied to dipolar particles in what follows. The torque contains both extrinsic and intrisic contributions,

$$\boldsymbol{\tau}(\omega) = \sum_j \boldsymbol{\tau}_j^i(\omega) + \boldsymbol{\tau}_j^e(\omega).$$

The intrinsic torque acting on particle j, which makes that particle spin around its own axis, reduces to

$$\boldsymbol{\tau}_j^i(\omega) = \frac{1}{\pi}\left[\mathrm{Re}\left\{\mathbf{p}_j \times \mathbf{E}_j^*\right\} + \frac{2k^3}{3}\mathrm{Im}\left\{\mathbf{p}_j \times \mathbf{p}_j^*\right\}\right],$$

whereas the extrinsic component, which contributes to rotations of the cluster as a whole, is

$$\boldsymbol{\tau}_j^e(\omega) = \mathbf{r}_j \times \mathbf{F}_j(\omega).$$

Also, the force on particle j can be written as

$$\mathbf{F}_j(\omega) = \frac{1}{\pi}\sum_{\beta=x,y,z} \mathrm{Re}\left\{p_{j,\beta}\nabla E_{j,\beta}^*\right\}.$$

In these expressions, $\mathbf{p}_j$ is the 3D dipole vector of particle j, which corresponds to component j of Eq. (B5), whereas

$$\mathbf{E}_j(\omega) = \sum_{j'}\left(\frac{\mathbf{1}}{1-\alpha\,\mathcal{G}^0}\right)_{jj'} \cdot \mathbf{E}_{j'}^{\mathrm{ext}}$$

and $\mathbf{E}_{j'}^{\mathrm{ext}}$ is the external electron field. The latter is computed from Eq. (B6) using the electron current

$$\mathbf{j}(\mathbf{r},\omega) = \frac{2\pi \mathrm{i}\hbar e}{m_e}\psi_f^*(\mathbf{r})\nabla\psi_i(\mathbf{r})\delta(\omega - \varepsilon_i + \varepsilon_f).$$

In the non-retarded limit, radiation corrections can be neglected, so that the transfer of linear momentum along z has to coincide with the time-integral of the force in that direction. A detailed balance expression can be written in frequency components as

$$F_z(\omega) = \frac{\hbar\omega}{v}\Gamma(\omega). \tag{10}$$

Additionally, the angular momentum transfer to the cluster, obtained from the integral of $\boldsymbol{\tau}(\omega)$ over the whole ω spectrum, should exactly cancel the orbital momentum gain of the electron. For an incident electron without a net orbital angular momentum, conservation of the z component requires to satisfy the condition

$$\tau_z(\omega) = -\hbar m \Gamma(\omega). \tag{11}$$

We have analytically corroborated Eqs. (10) and (11) for a single particle. For clusters consisting of several particles, the algebra becomes rather involved, but we have numerically verified them up to the computer numerical precision. Finally, we note that the extrinsic torque generally dominates the transfer to chiral clusters similar to those considered in this work, as illustrated for a particular case in Fig. S4(d). However, the relative contributions of intrinsic and extrinsic torques are very dependent on geometry. Incidentally, we have focused on forces and torques along z, which are relevant to the present study, although a similar analysis could be carried out for x and y components in connection to lateral deflections of the electron.

II. CHIRAL MOLECULE

A. Inelastic electron transition probability for a chiral molecule

The energy-loss probability for a chiral molecule placed at the position $\mathbf{r}_0$ with respect to the origin of the electron vortex can be obtained from Eqs. (2) and (3), in which the Green tensor is now given by Eq. (D2) (see Appendix D). We find

$$h(\mathbf{R},\mathbf{R}',\omega) = \frac{e^2}{\pi\hbar\omega^2}\int dz\, dz'\, \mathrm{e}^{-\mathrm{i}q_z(z-z')}\,\mathrm{Im}\left\{\mathbf{T}^{\mathrm{T}}(\mathbf{r}-\mathbf{r}_0,\omega)\cdot\mathfrak{a}\cdot\mathbf{T}(\mathbf{r}_0-\mathbf{r}',\omega)\right\},$$

where $\mathfrak{a}$ is a 6×6 generalized polarizability matrix derived in Appendix C and $\mathbf{T}(\mathbf{r}_0-\mathbf{r}',\omega)$ is a 6-component vector obtained by projecting the electric-electric induced Green tensor on the $\hat{\mathbf{z}}$ direction (i.e., along the electron beam). More precisely,

$$\mathbf{T}(\mathbf{r}_0-\mathbf{r}',\omega) = \begin{bmatrix} \hat{\mathbf{x}}\cdot\mathcal{G}^0_{EE}(\mathbf{r}_0-\mathbf{r}',\omega)\cdot\hat{\mathbf{z}} \\ \hat{\mathbf{y}}\cdot\mathcal{G}^0_{EE}(\mathbf{r}_0-\mathbf{r}',\omega)\cdot\hat{\mathbf{z}} \\ \hat{\mathbf{z}}\cdot\mathcal{G}^0_{EE}(\mathbf{r}_0-\mathbf{r}',\omega)\cdot\hat{\mathbf{z}} \\ \hat{\mathbf{x}}\cdot\mathcal{G}^0_{ME}(\mathbf{r}_0-\mathbf{r}',\omega)\cdot\hat{\mathbf{z}} \\ \hat{\mathbf{y}}\cdot\mathcal{G}^0_{ME}(\mathbf{r}_0-\mathbf{r}',\omega)\cdot\hat{\mathbf{z}} \\ \hat{\mathbf{z}}\cdot\mathcal{G}^0_{ME}(\mathbf{r}_0-\mathbf{r}',\omega)\cdot\hat{\mathbf{z}} \end{bmatrix}.$$

Following an almost identical derivation as the one in Sec. I A, and taking into account the symmetries of the free-space Green functions, we obtain a similar expression as Eq. (4) for the loss probability,

$$\Gamma(\omega) = \frac{4e^2q_z^2}{\pi\hbar v^2\gamma^2}\sum_{f_\perp}\mathrm{Im}\{\mathbf{N}^+\cdot\mathfrak{a}\cdot\mathbf{N}\},$$

where the 6-component vector $\mathbf{N} = [\mathbf{N}_{EE},\ \mathbf{N}_{ME}]$ has both electric and crossed electric-magnetic components,

$$\mathbf{N}_{EE} = \int d^2\mathbf{R}\ \psi^*_{f\perp}(\mathbf{R})\psi_{i\perp}(\mathbf{R})\ \left[\frac{(\mathbf{R}-\mathbf{R}_0)}{|\mathbf{R}-\mathbf{R}_0|}K_1\left(\frac{q_z|\mathbf{R}-\mathbf{R}_0|}{\gamma}\right) + \hat{\mathbf{z}}\frac{\mathrm{i}}{\gamma}K_0\left(\frac{q_z|\mathbf{R}-\mathbf{R}_0|}{\gamma}\right)\right],$$
$$\mathbf{N}_{ME} = \hat{\mathbf{z}}\times\left[\frac{v}{c}\int d^2\mathbf{R}\ \psi^*_{f\perp}(\mathbf{R})\psi_{i\perp}(\mathbf{R})\ K_1\left(\frac{q_z|\mathbf{R}-\mathbf{R}_0|}{\gamma}\right)\ \frac{(\mathbf{R}-\mathbf{R}_0)}{|\mathbf{R}-\mathbf{R}_0|}\right].$$

We now apply this formula to study the transition from an electron plane wave to a m_f vortex beam. The loss cross-section is formally equivalent to the one obtained for the cluster of spheres,

$$\sigma_{m_f}(\omega) = \frac{8e^2q_z^2}{\hbar v^2\gamma^2}\int_0^\infty P_f\, dP_f \mathrm{Im}\left\{\mathbf{M}^+\cdot\mathfrak{a}\cdot\mathbf{M}\right\},$$

but here the polarizability corresponds to the chiral molecule and the components of vector $\mathbf{M} = [\mathbf{M}_{EE},\ \mathbf{M}_{ME}]$ are

$$\begin{aligned}
\mathbf{M}_{EE} &= \left[g_1\ K'_{m_f}\left(\frac{q_z R_0}{\gamma}\right) + g_2\ I'_{m_f}\left(\frac{q_z R_0}{\gamma}\right)\right]\hat{R}_0 \\
&\quad + \left[g_1\ K_{m_f}\left(\frac{q_z R_0}{\gamma}\right) + g_2\ I_{m_f}\left(\frac{q_z R_0}{\gamma}\right)\right] \mathrm{i}\left(\frac{-m_f\gamma}{R_0 q_z}\hat{\varphi}_0 + \frac{1}{\gamma}\hat{z}_0\right), \\
\mathbf{M}_{ME} &= \frac{v}{c}\left[g_1\ K_{m_f}\left(\frac{q_z R_0}{\gamma}\right) + g_2\ I_{m_f}\left(\frac{q_z R_0}{\gamma}\right)\right] \mathrm{i}\frac{m_f\gamma}{R_0 q_z}\hat{R}_0 + \frac{v}{c}\left[g_1\ K'_{m_f}\left(\frac{q_z R_0}{\gamma}\right) + g_2\ I'_{m_f}\left(\frac{q_z R_0}{\gamma}\right)\right]\hat{\varphi}_0,
\end{aligned} \tag{12}$$

where g_1 and g_2 are defined in Eqs. (7).

These expressions are used to produce the results shown for molecules in the main paper.

B. Dichroism as a function of the crossed electric-magnetic terms in the polarizability

In the following, we show that the dichroism only depends on the crossed electric-magnetic components of the polarizability, and more precisely, on the scalar product between the electric and magnetic dipoles. For simplicity, we consider a molecule with an electric dipole $\mathbf{p}_{eg} = p_{eg}\hat{\mathbf{x}}$ oriented along $\hat{\mathbf{x}}$ and a magnetic dipole with components along all possible directions, $\mathbf{m}_{eg} = m_{eg,x}\hat{\mathbf{x}} + m_{eg,y}\hat{\mathbf{y}} + m_{eg,z}\hat{\mathbf{z}}$. The only nonzero terms of $\alpha_{EM}(\omega)$ are then

$$\alpha_{EM}^{x\beta} = \frac{p_{eg} m_{eg,\beta}}{\hbar}\left[\frac{1}{\omega_0 - \omega - \mathrm{i}\gamma_0/2} - \frac{1}{\omega_0 + \omega + \mathrm{i}\gamma_0/2}\right],$$

where $\beta = x, y, z$. From here, we find

$$\begin{aligned}
\mathbf{M}^+ \cdot \mathfrak{a} \cdot \mathbf{M} =& \alpha_{EE}^{xx}\,|M_{EE}^x|^2 + \alpha_{MM}^{xx}\,|M_{ME}^x|^2 + \alpha_{MM}^{yy}\,|M_{ME}^y|^2 \\
&+2\,\alpha_{MM}^{xy}\,\mathrm{Re}\{(M_{ME}^x)^* M_{ME}^y\} \\
&+2\,\mathrm{i}\,\alpha_{EM}^{xy}\,\mathrm{Im}\{M_{ME}^y (M_{EE}^x)^*\} \\
&+2\,\mathrm{i}\,\alpha_{EM}^{xx}\,\mathrm{Im}\{M_{ME}^x (M_{EE}^x)^*\},
\end{aligned} \tag{13}$$

where only the last term is odd with respect to m_f (i.e., it is the only one that produces dichroism). Inserting $\mathbf{M}_{ME}$ [Eq. (12)] into Eq. (13), the dichroism reduces to

$$\sigma_{m_f}(\omega) - \sigma_{-m_f}(\omega) = \frac{32 e^2 q_z}{\hbar v c \gamma R_0}\ m_f\ \mathrm{Re}\{\alpha_{EM}^{xx}\}\ \mathcal{F}(R_0, \omega),$$

where

$$\mathcal{F}(R_0,\omega) = \int_0^\infty P_f\, dP_f \left[g_1\ K'_{m_f}\left(\frac{q_z R_0}{\gamma}\right) + g_2\ I'_{m_f}\left(\frac{q_z R_0}{\gamma}\right)\right]\left[g_1\ K_{m_f}\left(\frac{q_z R_0}{\gamma}\right) + g_2\ I_{m_f}\left(\frac{q_z R_0}{\gamma}\right)\right].$$

As expected, this only depends on the scalar product $\mathbf{p}_{eg} \cdot \mathbf{m}_{eg}$ (i.e., the crossed electric-magnetic polarizability).

Appendix A: Polarizability of a spherical particle

In this work, we consider identical homogeneous spherical particles represented through their scalar polarizability. We calculate the latter from the dipolar electric Mie scattering coefficient as

$$\alpha(\omega) = \frac{3c^3}{2\omega^3}\frac{-j_1(\rho_0)\,[\rho_1 j_1(\rho_1)]' + \epsilon\,[\rho_0 j_1(\rho_0)]'\,j_1(\rho_1)}{h_1^{(+)}(\rho_0)\,[\rho_1 j_1(\rho_1)]' - \epsilon\left[\rho_0 h_1^{(+)}(\rho_0)\right]'\,j_1(\rho_1)},$$

where ϵ is the permittivity of the particle, a is the radius, $j_1(x) = (\sin x)/x^2 - (\cos x)/x$ and $h_1^{(+)}(x) = (1/x^2 - \mathrm{i}/x)\mathrm{e}^{\mathrm{i}x}$ are spherical Bessel and Hankel functions, respectively, $\rho_0 = \omega a/c$, $\rho_1 = \sqrt{\epsilon}\rho_0$, and the prime denotes differentiation with respect to the argument.

Appendix B: Electromagnetic Green tensor of a small-particle cluster

The electromagnetic Green tensor $\mathcal{G}$ describes the response of a structure to external sources. More precisely, we define it in frequency space ω through the relation

$$\mathbf{E}(\mathbf{r},\omega) = \frac{\mathrm{i}}{\omega}\int d^3\mathbf{r}'\,\mathcal{G}(\mathbf{r},\mathbf{r}',\omega)\cdot\mathbf{j}(\mathbf{r}',\omega) \tag{B1}$$

between an external current density $\mathbf{j}(\mathbf{r},\omega)$ and the electric field that it generates. We intend to obtain a general expression for $\mathcal{G}$ in the presence of small particles placed at positions $\mathbf{r}_j$ and described through their (identical) polarizability $\alpha(\omega)$.

First, we note that the current associated with an individual dipole $\mathbf{p}_j$ at position $\mathbf{r}_j$ is $-\mathrm{i}\omega\mathbf{p}_j\delta(\mathbf{r}-\mathbf{r}_j)$, so that according to Eq. (B1) the electric field produced by that dipole reduces to

$$\mathcal{G}^0(\mathbf{r}-\mathbf{r}_j,\omega)\cdot\,\mathbf{p}_j, \tag{B2}$$

where

$$\mathcal{G}^0(\mathbf{r},\omega) = \left(k^2\mathfrak{I}+\nabla\otimes\nabla\right)\frac{\mathrm{e}^{\mathrm{i}kr}}{r} \tag{B3}$$

is the vacuum Green tensor, $k=\omega/c$, and $\mathfrak{I}$ is the 3×3 unit matrix. For a particle cluster, we can write the self-consistent dipole at particle j in response to an externally applied field $\mathbf{E}_j^{\mathrm{ext}}=\mathbf{E}^{\mathrm{ext}}(\mathbf{r}_j,\omega)$ as

$$\mathbf{p}_j = \alpha\left(\mathbf{E}_j^{\mathrm{ext}}+\sum_{j'\neq j}\mathcal{G}^0_{jj'}\cdot\mathbf{p}_{j'}\right), \tag{B4}$$

where

$$\mathcal{G}^0_{jj'} = \mathcal{G}^0(\mathbf{r}_j-\mathbf{r}_{j'},\omega).$$

The sum in Eq. (B4) represents the field produced at $\mathbf{r}_j$ by dipoles other than j. It is useful to note that this expression can be straightforwardly applied to describe samples of arbitrary shape, in the spirit of the so-called discrete-dipole approximation (DDA) [3]. We use matrix notation throughout this work, with matrix indices running over the three Cartesian directions for each and all of the particles j. In particular, Eq. (B4) can be recast as

$$\mathbf{p} = \frac{\mathbf{1}}{\alpha^{-1}-\mathcal{G}^0}\cdot\mathbf{E}^{\mathrm{ext}}. \tag{B5}$$

Now, considering the external field

$$\mathbf{E}_j^{\mathrm{ext}} = \frac{\mathrm{i}}{\omega}\int d^3\mathbf{r}\,\mathcal{G}^0(\mathbf{r}_j-\mathbf{r},\omega)\cdot\mathbf{j}(\mathbf{r},\omega) \tag{B6}$$

produced by the current $\mathbf{j}$, calculating the self-consistently induced dipoles from Eq. (B4), and summing the dipole fields given by Eq. (B2), we finally obtain an expression identical to Eq. (B1) with

$$\mathcal{G}(\mathbf{r},\mathbf{r}',\omega) = \sum_{jj'}\mathcal{G}^0(\mathbf{r}-\mathbf{r}_j,\omega)\cdot\left(\frac{\mathbf{1}}{\alpha^{-1}-\mathcal{G}^0}\right)_{jj'}\cdot\,\mathcal{G}^0(\mathbf{r}_{j'}-\mathbf{r}',\omega). \tag{B7}$$

Appendix C: Polarizability of a chiral molecule

In this appendix, we derive expressions for the electric and magnetic polarizabilities of a chiral molecule. We consider transitions between the ground $|g\rangle$ and excited $|e\rangle$ quantum states of the molecule, with resonant frequency $\omega_0=\varepsilon_e-\varepsilon_g$. The system Hamiltonian H consists of a free term and an interaction term

$$H_{\mathrm{int}} = -\mathbf{p}\cdot\mathbf{E}-\mathbf{m}\cdot\mathbf{H},$$

where $\mathbf{E}$ and $\mathbf{H}$ correspond to the external classical electromagnetic field at the position of the molecule, which for simplicity we take to be monochromatic,

$$\mathbf{E} = \mathbf{E}(\omega)\, e^{-\mathrm{i}\omega t} + \mathbf{E}^*(\omega)\, e^{\mathrm{i}\omega t},$$
$$\mathbf{H} = \mathbf{H}(\omega)\, e^{-\mathrm{i}\omega t} + \mathbf{H}^*(\omega)\, e^{\mathrm{i}\omega t}.$$

Our results can be trivially extended to polychromatic fields. The molecule wave function is a superposition of ground and excited states,

$$|\psi(t)\rangle = c_g(t)\, e^{-\mathrm{i}\varepsilon_g t}\, |g\rangle + c_e(t)\, e^{-\mathrm{i}\varepsilon_e t}\, |e\rangle\,.$$

Inserting this expresssion into Schrödinger's equation $\mathrm{i}\hbar\partial_t\, |\psi(t)\rangle = H\, |\psi(t)\rangle$, the coefficients $c_{g,e}(t)$ are found to satisfy the equations

$$\dot{c}_g(t) = \frac{\mathrm{i}}{\hbar} c_e(t)\, [\mathbf{p}_{ge}\cdot\mathbf{E}(\omega) + \mathbf{m}_{ge}\cdot\mathbf{H}(\omega)]\, e^{-\mathrm{i}(\omega+\omega_0)t} + \frac{\mathrm{i}}{\hbar} c_e(t)\, [\mathbf{p}_{ge}\cdot\mathbf{E}^*(\omega) + \mathbf{m}_{ge}\cdot\mathbf{H}^*(\omega)]\, e^{\mathrm{i}(\omega-\omega_0)t},$$
$$\dot{c}_e(t) = \frac{\mathrm{i}}{\hbar} c_g(t)\, [\mathbf{p}_{eg}\cdot\mathbf{E}(\omega) + \mathbf{m}_{eg}\cdot\mathbf{H}(\omega)]\, e^{-\mathrm{i}(\omega-\omega_0)t} + \frac{\mathrm{i}}{\hbar} c_g(t)\, [\mathbf{p}_{eg}\cdot\mathbf{E}^*(\omega) + \mathbf{m}_{eg}\cdot\mathbf{H}^*(\omega)]\, e^{\mathrm{i}(\omega+\omega_0)t},$$

where

$$\mathbf{p}_{eg} = \langle e|\mathbf{p}|g\rangle = -e\,\langle e|\mathbf{r}|g\rangle\,,$$
$$\mathbf{m}_{eg} = \langle e|\mathbf{m}|g\rangle = -\frac{e}{2m_e c}\,\langle e|\mathbf{L}|g\rangle = \frac{\mathrm{i}e\hbar}{2m_e c}\,\langle e|\mathbf{r}\times\nabla|g\rangle$$

are the electric and magnetic transition matrix elements. The linear response polarizabilities are obtained from first-order perturbation theory (i.e., setting $c_g = 1$ and $c_e = 0$ in the right-hand side of the above equations). The amplitude of the excited state reduces to

$$c_e(t) = -\frac{1}{\hbar}\frac{\mathbf{p}_{eg}\cdot\mathbf{E}(\omega) + \mathbf{m}_{eg}\cdot\mathbf{H}(\omega)}{\omega-\omega_0+\mathrm{i}\gamma_0/2} e^{-\mathrm{i}(\omega-\omega_0)t} + \frac{1}{\hbar}\frac{\mathbf{p}_{eg}\cdot\mathbf{E}^*(\omega) + \mathbf{m}_{eg}\cdot\mathbf{H}^*(\omega)}{\omega+\omega_0-\mathrm{i}\gamma_0/2} e^{\mathrm{i}(\omega+\omega_0)t},$$

where γ_0 is an effective decay rate. The expected values of the electric and magnetic dipoles are then

$$\langle\mathbf{p}(t)\rangle = -\frac{1}{\hbar}\frac{\mathbf{p}_{eg}\cdot\mathbf{E}(\omega)\mathbf{p}_{ge} + \mathbf{m}_{eg}\cdot\mathbf{H}(\omega)\mathbf{p}_{ge}}{\omega-\omega_0+\mathrm{i}\gamma_0/2}\, e^{-\mathrm{i}\omega t} + \frac{1}{\hbar}\frac{\mathbf{p}_{eg}\cdot\mathbf{E}^*(\omega)\mathbf{p}_{ge} + \mathbf{m}_{eg}\cdot\mathbf{H}^*(\omega)\mathbf{p}_{ge}}{\omega+\omega_0-\mathrm{i}\gamma_0/2}\, e^{\mathrm{i}\omega t} + \text{c.c.},$$
$$\langle\mathbf{m}(t)\rangle = -\frac{1}{\hbar}\frac{\mathbf{p}_{eg}\cdot\mathbf{E}(\omega)\mathbf{m}_{ge} + \mathbf{m}_{eg}\cdot\mathbf{H}(\omega)\mathbf{m}_{ge}}{\omega-\omega_0+\mathrm{i}\gamma_0/2}\, e^{-\mathrm{i}\omega t} + \frac{1}{\hbar}\frac{\mathbf{p}_{eg}\cdot\mathbf{E}^*(\omega)\mathbf{m}_{ge} + \mathbf{m}_{eg}\cdot\mathbf{H}^*(\omega)\mathbf{m}_{ge}}{\omega+\omega_0-\mathrm{i}\gamma_0/2}\, e^{\mathrm{i}\omega t} + \text{c.c.},$$

where c.c. stands for complex conjugate.

We now define the polarizability components from the expression

$$\mathbf{p}(t) = [\alpha_{EE}(\omega)\cdot\mathbf{E}(\mathbf{r},\omega) + \alpha_{EM}(\omega)\cdot\mathbf{H}(\mathbf{r},\omega)]\; e^{-\mathrm{i}\omega t} + \text{c.c.}, \tag{C1a}$$

$$\mathbf{m}(t) = [\alpha_{ME}(\omega)\cdot\mathbf{E}(\mathbf{r},\omega) + \alpha_{MM}(\omega)\cdot\mathbf{H}(\mathbf{r},\omega)]\; e^{-\mathrm{i}\omega t} + \text{c.c.} \tag{C1b}$$

Taking into account the hermiticity of $\mathbf{p}$ and $\mathbf{m}$, we finally obtain the 6×6 generalized polarizability matrix

$$\mathbb{\alpha} = \begin{bmatrix} \alpha_{EE} & \alpha_{EM} \\ \alpha_{ME} & \alpha_{MM} \end{bmatrix},$$

where

$$\alpha_{EE}(\omega) = \frac{1}{\hbar}\left[\frac{1}{\omega_0-\omega-\mathrm{i}\gamma_0/2} + \frac{1}{\omega_0+\omega+\mathrm{i}\gamma_0/2}\right]\mathbf{p}_{ge}\otimes\mathbf{p}_{eg}, \tag{C2a}$$

$$\alpha_{MM}(\omega) = \frac{1}{\hbar}\left[\frac{1}{\omega_0-\omega-\mathrm{i}\gamma_0/2} + \frac{1}{\omega_0+\omega+\mathrm{i}\gamma_0/2}\right]\mathbf{m}_{ge}\otimes\mathbf{m}_{eg}, \tag{C2b}$$

$$\alpha_{EM}(\omega) = \frac{1}{\hbar}\left[\frac{1}{\omega_0 - \omega - \mathrm{i}\gamma_0/2} - \frac{1}{\omega_0 + \omega + \mathrm{i}\gamma_0/2}\right] \mathbf{p}_{ge} \otimes \mathbf{m}_{eg}, \tag{C2c}$$

$$\alpha_{ME}(\omega) = -\alpha_{EM}^{T}(\omega). \tag{C2d}$$

Notice that the dichroism response originates in the crossed electric-magnetic terms α_{EM} and α_{ME}, and therefore, only non-orthogonal electric and magnetic dipoles produce chirality. It is thus convenient to express the dipole elements in terms of the strength of the electric dipole and the projection of the magnetic dipole on the electric one [4],

$$|\mathbf{p}_{ge}| = e r_{ge},$$
$$(\mathbf{p}_{ge} \cdot \mathbf{m}_{eg})/|\mathbf{p}_{ge}| = -\frac{\mathrm{i}e\omega_0 r_{eg} r_0}{2c}.$$

Finally, we calculate the extinction cross-section of the molecule from

$$\sigma^{ext}(\omega) = \frac{4\pi k}{|\mathbf{E}(\omega)|^2} \mathrm{Im}\left\{\mathbf{p}\,(\omega) \cdot \mathbf{E}^*(\omega) + \mathbf{m}\,(\omega) \cdot \mathbf{H}^*(\omega)\right\}$$

to obtain the optical dichroism shown in Fig. 3(d) of the main paper.

Appendix D: Electromagnetic Green tensor of a chiral molecule

We need to derive the electromagnetic Green tensor in the presence of a chiral particle (e.g., the molecule considered in Appendix C). We first write a generalization ot Eq. (B1) to describe the response of the particle to electric and magnetic external current densities $\mathbf{j}_E$ and $\mathbf{j}_M$ as

$$\mathbf{E}(\mathbf{r},\omega) = \frac{\mathrm{i}}{\omega}\int d^3\mathbf{r}'\, \mathcal{G}_{EE}(\mathbf{r},\mathbf{r}',\omega)\cdot \mathbf{j}_E(\mathbf{r}',\omega) + \frac{\mathrm{i}}{\omega}\int d^3\mathbf{r}'\, \mathcal{G}_{EM}(\mathbf{r},\mathbf{r}',\omega)\cdot \mathbf{j}_M(\mathbf{r}',\omega),$$
$$\mathbf{H}(\mathbf{r},\omega) = \frac{\mathrm{i}}{\omega}\int d^3\mathbf{r}'\, \mathcal{G}_{ME}(\mathbf{r},\mathbf{r}',\omega)\cdot \mathbf{j}_E(\mathbf{r}',\omega) + \frac{\mathrm{i}}{\omega}\int d^3\mathbf{r}'\, \mathcal{G}_{MM}(\mathbf{r},\mathbf{r}',\omega)\cdot \mathbf{j}_M(\mathbf{r}',\omega).$$

The currents associated with individual electric and magnetic dipoles $\mathbf{p}$ and $\mathbf{m}$ placed at position $\mathbf{r}_0$ are

$$\mathbf{j}_E(\mathbf{r},\omega) = -\mathrm{i}\,\omega\,\mathbf{p}\,\delta(\mathbf{r}-\mathbf{r}_0),$$
$$\mathbf{j}_M(\mathbf{r},\omega) = -\mathrm{i}\,\omega\,\mathbf{m}\,\delta(\mathbf{r}-\mathbf{r}_0),$$

so that the electric and magnetic fields produced by these dipoles reduce to

$$\mathbf{E}(\mathbf{r},\omega) = \mathcal{G}^0_{EE}(\mathbf{r}-\mathbf{r}_0,\omega)\cdot\mathbf{p} + \mathcal{G}^0_{EM}(\mathbf{r}-\mathbf{r}_0,\omega)\cdot\mathbf{m}, \tag{D1a}$$

$$\mathbf{H}(\mathbf{r},\omega) = \mathcal{G}^0_{ME}(\mathbf{r}-\mathbf{r}_0,\omega)\cdot\mathbf{p} + \mathcal{G}^0_{MM}(\mathbf{r}-\mathbf{r}_0,\omega)\cdot\mathbf{m}, \tag{D1b}$$

where

$$\mathcal{G}_{EE}(\mathbf{r}-\mathbf{r}_0,\omega) = \mathcal{G}_{MM}(\mathbf{r}-\mathbf{r}_0,\omega) = \mathcal{G}^0(\mathbf{r}-\mathbf{r}_0,\omega),$$
$$\mathcal{G}_{EM}(\mathbf{r}-\mathbf{r}_0,\omega) = -\mathcal{G}_{ME}(\mathbf{r}-\mathbf{r}_0,\omega) = -\frac{1}{\mathrm{i}k}\nabla\times\mathcal{G}^0(\mathbf{r}-\mathbf{r}_0,\omega),$$

and $\mathcal{G}^0(\mathbf{r},\mathbf{r}',\omega)$ is the vacuum Green tensor defined by Eq. (B3).

We can now write the dipoles induced by an external field using the polarizability as defined by Eqs. (C1), which can be combined with Eqs. (D1) to write the induced electric and magnetic fields as

$$\begin{bmatrix}\mathbf{E}(\mathbf{r},\omega)\\ \mathbf{H}(\mathbf{r},\omega)\end{bmatrix} = \frac{\mathrm{i}}{\omega}\int d^3\mathbf{r}'\, \mathcal{G}(\mathbf{r},\mathbf{r}',\omega)\cdot\begin{bmatrix}\mathbf{j}_E(\mathbf{r}',\omega)\\ \mathbf{j}_M(\mathbf{r}',\omega)\end{bmatrix}.$$

Then, the induced Green tensor is a 6×6 matrix,

$$\begin{aligned}\mathcal{G}(\mathbf{r},\mathbf{r}',\omega) &= \begin{bmatrix} \mathcal{G}_{EE}(\mathbf{r},\mathbf{r}',\omega) & \mathcal{G}_{EM}(\mathbf{r},\mathbf{r}',\omega) \\ \mathcal{G}_{ME}(\mathbf{r},\mathbf{r}',\omega) & \mathcal{G}_{MM}(\mathbf{r},\mathbf{r}',\omega) \end{bmatrix} \\ &= \begin{bmatrix} \mathcal{G}^0_{EE}(\mathbf{r}-\mathbf{r}_0,\omega) & \mathcal{G}^0_{EM}(\mathbf{r}-\mathbf{r}_0,\omega) \\ \mathcal{G}^0_{ME}(\mathbf{r}-\mathbf{r}_0,\omega) & \mathcal{G}^0_{MM}(\mathbf{r}-\mathbf{r}_0,\omega) \end{bmatrix} \cdot \mathbb{Q} \cdot \begin{bmatrix} \mathcal{G}^0_{EE}(\mathbf{r}_0-\mathbf{r}',\omega) & \mathcal{G}^0_{EM}(\mathbf{r}_0-\mathbf{r}',\omega) \\ \mathcal{G}^0_{ME}(\mathbf{r}_0-\mathbf{r}',\omega) & \mathcal{G}^0_{MM}(\mathbf{r}_0-\mathbf{r}',\omega) \end{bmatrix}. \end{aligned} \tag{D2}$$

Taking into account that the magnetic current generated by the moving electron is negligible, as it originates in motion within the transversal plane, in which the electron velocity is small, we only consider inelastic losses mediated by $\mathcal{G}_{EE}$.

Appendix E: Absorption bands of the α-helix

The polarizability of the α-helix in the 190-220 nm spectral region is dominated by three optical resonances, each of them contributing with a Lorentizian term like in Eqs. (C2). We summarize in the following table the parameters of these absorption bands as fitted to the measurements of Ref. [5]:

Band	$\hbar\omega_0$ (eV)	$\hbar\gamma_0$ (eV)	Polarization	r_{eg} (nm)	r_0 (nm)
1	6.53	0.5	$\pi \to \pi^*$, $\perp$	0.048	0.12
2	5.96	0.4	$\pi \to \pi^*$, $\parallel$	0.022	-0.22
3	5.64	0.4	$n \to \pi^*$, $\parallel$	0.01	-0.82

The magnetic dipole associated with each resonance is considered to be parallel to the electric one, as only that component of $\mathbf{m}$ produces dichroism. The orientation of these dipoles relative to the molecule long axis are given in the polarization entry of the above table. The results of the main paper are obtained for random orientations of the molecule, over which the intensities are averaged using a sufficiently large number of Euler angles.

[1] F. J. García de Abajo, Rev. Mod. Phys. **82**, 209 (2010).
[2] F. J. García de Abajo, Phys. Rev. B **60**, 6086 (1999).
[3] B. T. Draine and P. J. Flatau, J. Opt. Soc. Am. A **11**, 1491 (1994).
[4] A. O. Govorov, Z. F. P. Hernandez, J. M. Slocik, and R. R. Naik, Nano Lett. **10**, 1374 (2010).
[5] W. C. Johnson and I. Tinoco, J. Am. Chem. Soc. **94**, 4389 (1972).